Journal of Materials Chemistry A

ROYAL SOCIETY OF CHEMISTRY

PAPER

View Article Online
View Journal

Cite this: DOI: 10.1039/d5ta09357k

Correlating Li^+ jump pathways and vibrational properties in lithium aluminum germanium phosphate glasses

Chang Gyu Baek,[a] Young Hoon Rim,*[b] Jae-Hyeon Ko[c] and Yong Suk Yang *[a]

Received 18th November 2025
Accepted 5th February 2026

DOI: 10.1039/d5ta09357k

rsc.li/materials-a

Lithium aluminum germanium phosphate (LAGP) glass ceramics have attracted considerable attention as promising solid electrolytes for next-generation lithium batteries owing to their improved safety and thermal stability. Despite significant progress, fundamental questions regarding Li^+ hopping processes, effective charge carrier concentration, and carrier mobility in glassy systems remain unresolved. In this work, we investigate the fundamental relationship between fast lithium-ion transport and the network structure in xLi_2O–$0.25Al_2O_3$–$1.5GeO_2$–$1.5P_2O_5$ (xLi_2O-AGPO; $0.75 \leq x \leq 2.5$) glasses. The dc conductivity increases by nearly three orders of magnitude, from 1.73×10^{-9} S cm^{-1} ($x = 0.75$) to 1.67×10^{-6} S cm^{-1} ($x = 2.5$) at 50 °C, while the dc activation energy decreases with increasing Li_2O content. The effective charge carrier concentration is evaluated from the conductivity data, and the corresponding carrier mobility is estimated. The charge carrier concentration increases nearly proportionally with Li_2O content, whereas the carrier mobility exhibits an exponential increase, similar to the trend observed for the dc conductivity. These results indicate that the exponential enhancement of dc conductivity with increasing x is primarily governed by the increase in carrier mobility. The facile migration of Li^+ is attributed to fractal conduction pathways formed by non-bridging oxygen sites, which are generated through the depolymerization of the phosphate network.

1. Introduction

Li-ion batteries are increasingly in demand for applications ranging from portable electronic devices to electric vehicles and large-scale energy storage systems owing to their high energy density and long cycle life.[1,2] Recently, solid electrolytes for all-solid-state batteries have emerged as key components for advanced electrochemical energy storage technologies because of their enhanced safety, excellent chemical and thermal stability, long cycle life, and high energy density. Among the various classes of oxide ion conductors, lithium-ion conductors are considered promising electrolyte candidates for these applications.[3–5] In particular, NASICON-type glass-ceramic electrolytes with the composition $Li_{1.5}Al_{0.5}Ge_{1.5}(PO_4)_3$ (hereafter referred to as LAGP) have attracted considerable attention, as they exhibit a high ionic conductivity of $\sim 10^{-4}$ S cm^{-1} at room temperature, along with superior electrochemical stability and a wide electrochemical window.[6,7] The NASICON crystal structure is composed of PO_4 tetrahedra that share corner oxygen atoms with MO_6 octahedra (where M = Ge in $LiGe_2(PO_4)_3$). Partial substitution of Al^{3+} for Ge^{4+} in $LiGe_2(PO_4)_3$ results in the incorporation of additional Li^+ ions at the 36f sites to maintain charge neutrality. Consequently, the Li^+ concentration in the LAGP structure increases, leading to a significant enhancement of ionic conductivity from $\sim 10^{-8}$ to $\sim 10^{-4}$ S cm^{-1}.[8] Furthermore, it has been reported that ionic conductivity can be further improved by substituting cations with larger ionic radii than Ge^{4+} and Al^{3+}, which effectively enlarges the diffusion channels for Li^+ migration.[9]

Li *et al.* reported in an early publication that the ionic conductivity of $Li_{1+x}Ge_{2-x}Al_xP_3O_{12}$ ($R\bar{3}C$ structure) reaches a maximum value of 3.5×10^{-5} S cm^{-1} at room temperature for the composition $x = 0.5$ among the investigated compositions in the range $0.1 \leq x \leq 0.6$.[10] Although LAGP is regarded as one of the most promising solid electrolytes for lithium-ion batteries, its practical application is still limited by relatively low bulk and grain-boundary ionic conductivities. To further enhance the ionic conductivity, Xu *et al.* conducted a systematic study on NASICON-type LAGP-xLi_2O (x = 0.0–0.20) lithium-ion-conducting glass-ceramics. They demonstrated that the glass-ceramic sample with $x = 0.05$ exhibits the highest ionic conductivity, reaching 7.25×10^{-4} S cm^{-1} at room temperature.[7]

Pershina *et al.* investigated the effects of Al_2O_3 addition on the microstructure, molecular structure, and ionic conductivity

[a]Department of Nanoenergy Engineering, College of Nanoscience and Nanotechnology, Pusan National University, Busan 46241, Republic of Korea. E-mail: ysyang@pusan.ac.kr

[b]College of Liberal Arts, Semyung University, Jecheon, Chungbuk 27136, Republic of Korea. E-mail: yrim@semyung.ac.kr

[c]School of Semiconductor Display Technology, Nano Convergence Technology Center, Hallym University, Chuncheon-si, Gangwon-do 24252, Republic of Korea

of $LiGe_2(PO_4)_3$ glass-ceramics by synthesizing $Li_{1+x}Al_xGe_{2-x}(PO_4)_3$ ($0 \leq x \leq 0.65$) compositions.[11] They reported that the $Li_{1.5}Al_{0.5}Ge_{1.5}(PO_4)_3$ composition ($x = 0.5$) exhibits the highest lithium-ion conductivity, reaching 5.03×10^{-4} S cm^{-1} at 25 °C. In recent years, most studies have focused on the synthesis of LAGP glass-ceramics *via* glass crystallization. However, reported data on the phase composition of these conductors and their corresponding ionic conductivities remain inconsistent. This inconsistency arises because crystallization parameters strongly influence lithium-ion mobility, the fraction of residual amorphous phases, and the formation of microstructural defects such as cracks and pores, all of which have a significant impact on the ionic conductivity of the materials.

However, the development of crystalline solid electrolytes for lithium-ion batteries inevitably faces several challenges, including high grain-boundary resistance and difficulties in achieving sufficient densification. In this regard, glass-based electrolytes offer distinct advantages over sintered polycrystalline materials. For example, glass systems provide broad compositional flexibility, enable processing at relatively low fabrication temperatures through the appropriate selection of glass formers, and allow for the formation of nanocrystalline constituents with isotropic physical properties within the disordered network structure.[12–14]

In ion-conducting glasses, the lack of direct experimental data on charge carrier concentration and mobility has led to differing interpretations of the conduction mechanism, with the glassy systems being alternatively treated as strong or weak electrolytes.[15,16] Therefore, the independent determination of charge carrier concentration and mobility is of crucial importance for a comprehensive understanding of ionic conductivity mechanisms in glasses. Recently, Souquet *et al.* proposed a model in which ionic displacement arises from the migration of cationic pairs formed through partial dissociation, a process that is thermally activated.[17] Using the Almond–West formalism, Hairetdinov *et al.* estimated the concentration of free charge carriers in fast-ion-conducting glasses by assuming strong electrolyte behavior.[18] In addition, Marple *et al.* demonstrated that an atomistic interpretation of the crossover hopping frequency, ω_h, in Jonscher's universal dielectric response provides a consistent description of ionic transport in glasses.[19] In this framework, mobile ions are temporarily trapped in local cages and subsequently hop across percolation clusters. Nevertheless, the Almond–West approach has been criticized for being phenomenological rather than constituting a rigorous microscopic theory.

Bunde *et al.* proposed a dynamic structure model, in which the existence of percolative diffusion pathways leads to an exponential increase in ionic conductivity with increasing ion concentration.[20] Sidebottom *et al.* argued that the anomalous-diffusion model of ionic transport in $LiPO_3$ glass supports both the jump relaxation model and the Coulomb-interacting lattice model.[21] However, it was later shown that the estimated diffusion length scale in lithium phosphate glass is too short to be comparable with the characteristic hopping distances in glassy systems.

By applying bond-valence techniques in conjunction with reverse Monte Carlo (RMC) simulations to mixed-alkali phosphate glasses, Swenson and Adams suggested that the two types of alkali ions are randomly mixed and migrate through distinct low-dimensional conduction pathways.[22] Based on the RMC-produced structure model, Rim *et al.* derived Jonscher's universal conductivity expression by introducing fractional Klein-Kramers kinetic equations containing non-integer differential and integral operators, which lead to a modified fractional Rayleigh equation describing the time- and velocity-dependent dynamics of ion transport.[23]

In a previous study, Rim *et al.* reported that the addition of lithium oxide in xLi_2O–$2Fe_2O_3$–$3P_2O_5$ glasses enhances the depolymerization of the iron phosphate network, accompanied by the formation of non-bridging oxygen (NBO) species through the conversion of Q^2 units to Q^1 and Q^0 units.[24] Here, the notation Q^n represents the structural units of the glass network, where n denotes the number of bridging oxygens per tetrahedral unit. Alkali-ion transport in glassy systems occurs *via* a thermally activated hopping process under an applied electric field, where ions migrate between NBO sites through potential minima in the disordered network.[25] Within the energy landscape of the glass network, the depth of the potential wells is determined by Coulomb interactions between the alkali ions and the surrounding network structure.[26] At low alkali-ion concentrations, ion conduction is primarily governed by long-range Coulomb interactions between mobile ions, whereas at higher ion concentrations, structural modifications of the glass network play a dominant role in determining the conduction behavior.[26] However, Rim *et al.* also reported that the relatively low ionic conductivity of the lithium silicate glasses arises from the limited participation of Li^+ ions in transport through NBO sites.[27] Consequently, elucidating the mechanism of fast ion transport in mixed aluminum–germanium–phosphate glasses remains a significant challenge, as the different charge valences of lithium, aluminum, and germanium ions interact distinctly with the surrounding phosphate network, leading to complex structural modification that critically influences ionic transport.

Polycrystalline, nanocrystalline, and glass-ceramic forms of $Li_{1+x}Al_xGe_{2-x}P_3O_{12}$ ($x = 0.5$), which exhibit typical ionic conductivities on the order of $\sim 10^{-4}$ S cm^{-1}, can be produced *via* glass-based processing routes. Such glass-derived approaches offer distinct advantages, as key microstructural parameters, including crystal size, degree of crystallinity, and the volume fraction of the crystalline and residual glassy phases, can be precisely tailored. Establishing the fundamental properties of the glassy state is of significant scientific importance because structurally disordered glasses exhibit electrical, thermal, mechanical, chemical, and optical properties that differ markedly from those of structurally ordered crystalline materials. To date, numerous studies have investigated $Li_{1+x}Al_xGe_{2-x}P_3O_{12}$ in crystalline, glass-ceramic, and glassy forms; however, most of these investigations have been restricted to a substitution range of $x \approx 0.5$.

In the present work, we aim to synthesize LAGP-based glasses over a broader range of Li_2O contents, starting from $x = 0.5$ and systematically increasing x up to the compositional

limit at which a glassy phase can be maintained. The fundamental physical properties of the resulting glasses are investigated with particular emphasis on elucidating the relationships among ionic conductivity, effective charge carrier concentration, and mobility as functions of Li_2O content. In this study, lithium alumina germanium phosphate glasses with compositions xLi_2O–$0.25Al_2O_3$–$1.5GeO_2$–$1.5P_2O_5$ (xLi_2O-AGPO), where $0.75 \leq x \leq 2.5$, were prepared, and their electrical impedance and Raman spectroscopic properties were systematically examined. An anomalous enhancement of dc conductivity is observed in the xLi_2O–$0.25Al_2O_3$–$1.5GeO_2$–$1.5P_2O_5$ glass system. As x increases from 0.75 to 2.5, the dc conductivity increases by nearly three orders of magnitude, from 1.73×10^{-9} to 1.67×10^{-6} S cm^{-1}. Such an exponential increase in dc conductivity with increasing Li_2O content has rarely been reported in ionic glasses. The combined electrical and Raman spectroscopic results presented in this study provide valuable insights into the design of glassy and glass-ceramic electrolytes with enhanced ionic conductivity.

The processes of ionic conduction and relaxation in xLi_2O-AGPO glasses are analyzed using Cole–Cole power-law representations. The effective concentration of mobile ionic charge carriers is evaluated, and the corresponding mobility is estimated from the dc conductivity. Furthermore, the origin of Li^+ transport is revealed by correlating Li^+ jump pathways with structural modifications of the glassy network. The present work provides a comprehensive understanding of ion dynamics in these glasses, offering valuable insights for both fundamental research and the development of high-performance electrochemical energy storage materials.

2. Experimental

AR-grade chemicals Li_2CO_3, Al_2O_3, GeO_2, and $NH_4H_2PO_4$ were used as starting materials to prepare lithium aluminum germanium phosphate glasses. The raw materials were thoroughly mixed for 1 h in an alumina bowl according to the molar ratio $xLi_2CO_3 : 0.25Al_2O_3 : 1.5GeO_2 : 3.0NH_4H_2PO_4$ (xLi_2O-AGPO; $x = 0.75, 1.0, 1.25, 1.5, 1.75, 2.0, 2.5$). Each batch was transferred into a platinum crucible and pre-annealed at 700 °C for 1 h in an electric furnace to remove volatile species such as CO_2 and NH_3. After cooling to room temperature, the annealed samples were reground for an additional 1 h to ensure compositional homogeneity.

The reground powders were subsequently melted in a platinum crucible at temperatures between 1200 and 1300 °C. The resulting melts were quenched by pressing between metal plates to obtain bulk glass samples. The quenched bulk glasses were transparent, with a typical thickness of approximately 0.06 cm.

To prepare thin glass samples suitable for impedance measurements, the bulk glasses were crushed, remelted at 1200–1300 °C, and rapidly quenched using a twin-roller technique. The thickness of the resulting glass sheets ranged from 5.8×10^{-3} to 7.7×10^{-3} cm, as measured using a digital micrometer with a precision of $\pm 5.0 \times 10^{-5}$ cm.

The amorphous nature of the samples was confirmed by X-ray diffraction (XRD) using a Miniflex II diffractometer (Rigaku, Japan) with a CuKα radiation ($\lambda = 1.5406$ Å). XRD patterns were recorded over the 2θ range of 10–80° with a step width of 0.05° and a counting time of 3 s per step.

Complex impedance measurements were carried out using an impedance analyzer (4294A, Keysight, U.S.A.). Circular gold electrodes with a radius of 0.15 cm were deposited on both sides of each sample, and gold leads were attached using silver paste. To remove organic components from the silver paste, the samples were heat-treated at 300 °C for 10 min. Impedance spectra were collected over a frequency range of 100 Hz to 30 MHz. Electrical measurements were performed in a temperature-controlled furnace from room temperature to 240 °C with a heating rate of 2 °C min^{-1}.

Raman spectra were obtained using a micro-Raman spectrometer (LabRAM HR Evolution, Horiba). Excitation was provided by a diode-pumped solid-state laser with a wavelength of 532 nm and an output power of approximately 9 mW. Raman measurements were conducted on small fragments of heat-treated samples. Spectra were recorded over the Raman shift range of 20–1400 cm^{-1} with an integration time of 10 s for each spectrum.

3. Results and discussion

3.1. Impedance analysis

Fig. 1 shows the typical XRD patterns of xLi_2O-AGPO ($x = 0.75$, 1.0, 1.25, 1.5, 1.75, 2.0, 2.5) glasses at 50 °C. The XRD patterns exhibit a wide halo without crystalline sharp Bragg peaks in the range of 10–80°, which is characteristic of the amorphous state. The scanning process was repeated 8 times, and then the XRD data were taken as an average.

The complex impedance spectra have been calculated using experimentally measured values of the dielectric constant and dielectric loss tangent as

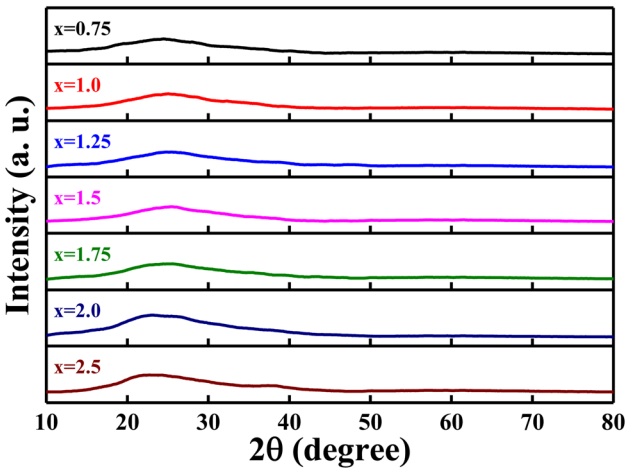

Fig. 1 XRD patterns of xLi_2O-AGPO ($x = 0.75$, 1.0, 1.25, 1.5, 1.75, 2.0, 2.5) glasses at 50 °C. XRD patterns have no Bragg peaks related to the crystalline phase, implying that the quenched samples are glasses.

$$Z^*(\omega) = \frac{1}{\omega\varepsilon_0\varepsilon_r'} \times \frac{d}{A} \times \frac{\tan\delta - i}{1 + \tan^2\delta} = Z' - iZ'', \quad (1)$$

where $\varepsilon_r'(\omega)$ is the real part of the relative dielectric constant, ε_0 is the vacuum permittivity, ω is the angular frequency, and $\tan\delta = \frac{\varepsilon_r''}{\varepsilon_r'}$ is the loss tangent factor. The loss tangent factor represents the ratio of the energy dissipated per radian in the dielectric to the energy stored. The electrode area is fixed at $A = \pi(0.15)^2$ cm^2 for all samples, while the sample thickness d ranges from 5.8×10^{-3} cm ($x = 1.25$) to 7.7×10^{-3} cm ($x = 0.75$).

The complex Cole–Cole formalism is one method for understanding the electrical response to the applied field. In particular, it is useful to understand how ions move through a broad distribution of random energy barriers. The Cole–Cole impedance is expressed as follows:[28]

$$Z^* = \frac{\Delta R}{1 + (i\omega\tau)^\gamma}, \quad (2)$$

where $Z^* = Z' - iZ''$, $\Delta R \cong R_0 - R_\infty$, R_0 and R_∞ are the resistances at zero and infinity of frequency, and τ and ω are the relaxation time and the applied field frequency, respectively. An exponent γ, the weight of the distribution of relaxation time, exists within $0 \le \gamma \le 1$. In the Debye system, the value of γ approaches 1, in which the complex impedance plot displays a perfect semicircle. The value of γ decreases if the relaxation time distribution increases, and the corresponding complex impedance plot shows a depressed semicircle. In a glass system, there is a structural disorder because of the inherent property and the various interionic Coulomb interactions. It appears as a non-Debye type value of the exponent, originating from the wide distribution of potential energy barriers.[25]

Fig. 2(a) represents the compositional dependence of complex impedance Cole–Cole spectra measured at 50 °C for several xLi$_2$O-AGPO glasses. In the inset in Fig. 2(a), the equivalent R-CPE parallel circuit is shown. Based on the impedance expression

$$Z^* = \frac{1}{\frac{1}{R} + Q(i\omega)^\beta}, \quad (3)$$

the impedance spectrum for $x = 0.75$ is fitted with the parameters $R = 62.8$ MΩ, $\beta = 0.78$ and $Q = 9.75 \times 10^{-11}$ Ω^{-1} s$^{0.78}$.[29]

A depressed semicircle arc of the complex impedance spectra intersects the Z′ axis on the low-frequency side when the impedance is extrapolated with the Cole–Cole formula, as seen for $x = 1.25$ in Fig. 2(a). This real part of complex impedance is defined by Z_0' and it gives the dc conductivity from the Cole–Cole representation in eqn (2), that is, $\sigma_{dc}^c = \frac{d}{Z_0 A}$. The obtained value of the impedance at the intersection is Z_0' ($x = 0.75$) = 6.28×10^7 Ω at 50 °C, and it decreases to Z_0' ($x = 2.5$) = 6.32×10^4 Ω at the same temperature, indicating that the dc conductivity increases rapidly with increasing concentration of lithium content. Namely, the dc conductivity σ_{dc}^c ($x = 0.75$) = 1.60×10^{-9} S cm^{-1} increases to σ_{dc}^c ($x = 2.5$) = 1.58×10^{-6} S cm^{-1}, showing that the conductivity increases exponentially with increasing x content.

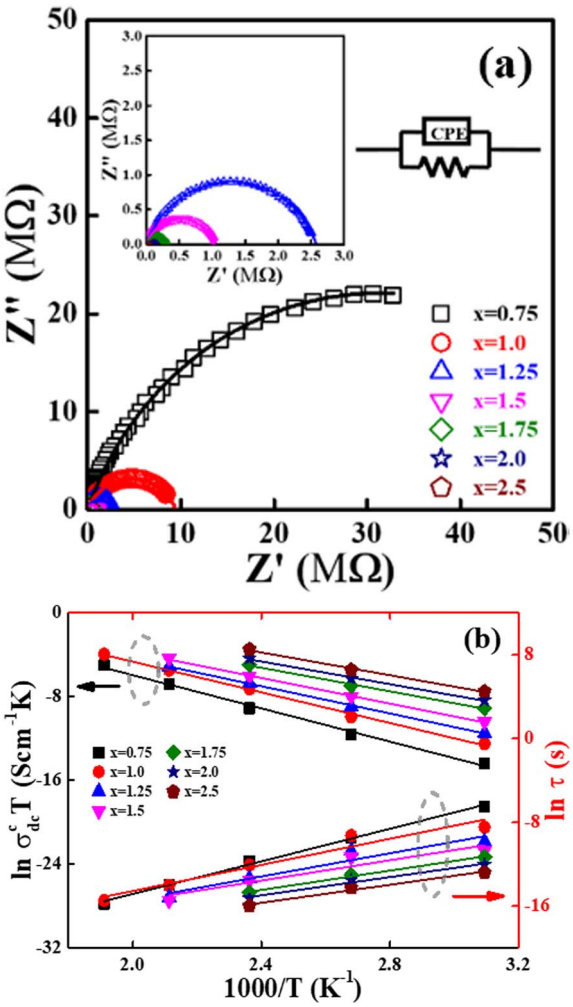

Fig. 2 Impedance analysis; (a) complex impedance plane plot with Cole–Cole fitting of xLi$_2$O-AGPO (x = 0.75, 1.0, 1.25, 1.5, 1.75, 2.0, 2.5) glasses at 50 °C. The insets show the magnified view and a R-CPE parallel equivalent circuit for x = 0.75. (b) The dc conductivity and relaxation time with the inverse temperature. The solid lines represent the fits with the Arrhenius relationships $\sigma_{dc}^c = C\exp\left(-\frac{E_{dc}^c}{k_B T}\right)$ and $\tau = \tau_0\exp\left(-\frac{E_m}{k_B T}\right)$, where E_{dc}^c and E_m are the dc and relaxation time activation energies, respectively.

The calculated exponent γ in eqn (2) varies slightly from 0.81 ($x = 0.75$) to 0.78 ($x = 2.5$) at various temperatures. The result indicates that the relaxation time distribution increases with increasing x content in xLi$_2$O-AGPO glasses.

Fig. 2(b) shows that the dc conductivity σ_{dc}^c obtained from the Cole–Cole formula obeys the Arrhenius relationship such as $\sigma_{dc}^c T = C'\exp\left(-\frac{E_{dc}}{k_B T}\right)$, where C' is a constant and k_B is the Boltzmann constant. The slope of the least-squares straight-line fits represents the value of the activation energies. The Arrhenius relationship indicates that the charge carriers contributing to dc conductivity are thermally activated. The obtained dc

activation energy decreases from $E_{dc}^{c} = 0.68$ eV ($x = 0.75$) to $E_{dc}^{c} = 0.46$ eV ($x = 2.5$), indicating that the average heights of the energy barrier for ion movements decrease with increasing Li_2O content.

In Fig. 2(b), we also present the relaxation time τ, obtained from the impedance Cole–Cole plot as a function of 1000/T. The relaxation time is obtained with ω_m, which denotes the frequency at which the imaginary part of the impedance, Z'' (dissipation), reaches its maximum in the impedance plane plot, satisfying the relationship $\omega_m\tau = 1$.[28] As seen in the figure, the relaxation time exponentially decreases from 1.5×10^{-3} s ($x = 0.75$) to 1.2×10^{-6} s ($x = 2.5$) at 50 °C with Li_2O content. This indicates that the time requirement to move between average hopping distances becomes shorter with the increase of x content, *i.e.*, ions move faster with larger x. The slope of ln τ *versus* $1/T$ decreases linearly with T. The relaxation time τ can be expressed as $\tau = \tau_0 \exp(E_m/k_BT)$, where E_m is the energy at the frequency, where the dissipation is maximum. The calculated E_m energy of the xLi_2O-AGPO glasses decreases from $E_m = 0.67$ eV ($x = 0.75$) to $E_m = 0.37$ eV ($x = 2.5$). The energy E_m is often referred to as migration or motional energy inside the network, where low migration energies lead to high ionic mobility. Therefore, the exponentially increasing dc conductivity and the lowering of the energy barriers are the origin of the exponentially increasing mobility in the xLi_2O-AGPO glasses.

3.2. Conductivity: charge carrier density and mobility

The frequency-dependent conductivity $\sigma(\omega)$ is calculated from the measured dielectric constant and dielectric loss tangent according to

$$\sigma(\omega) = \omega\varepsilon_0\varepsilon_r' \tan\delta, \text{ with } \tan\delta = \frac{\varepsilon_r''}{\varepsilon_r'}. \quad (4)$$

The conductivity spectra are analyzed using Jonscher's universal power law, separating the frequency-independent dc conductivity σ_{dc} and frequency-dependent ac conductivity σ_{ac} contributions. The fitting procedure has been carried out using[25]

$$\sigma(\omega) = \sigma_{dc} + \sigma_{ac} = \sigma_{dc}\left(1 + \left(\frac{\omega}{\omega_h}\right)^{s}\right). \quad (5)$$

The nearly constant loss (NCL) term proportional to ω is not observed in the present xLi_2O-AGPO glasses.[30] It is noted that ω_h is the crossover onset frequency from dc conductivity to ac conductivity, defined by $\sigma(\omega_h) = 2\sigma_{dc}$, and the exponent s is a dimensionless constant $0 \le s \le 1$ for ionic glass.

The compositional dependence of the frequency-dependent conductivity, $\sigma(\omega)$, measured at 50 °C for various xLi_2O-AGPO glass samples is presented in Fig. 3(a). The inset shows the conductivity spectra for the $x = 0.75$ sample measured at different temperatures. We have observed that the dc conductivity $\sigma_{dc} = 1.73 \times 10^{-9}$ S cm^{-1} for $x = 0.75$ increases to 1.67×10^{-6} S cm^{-1} for $x = 2.5$, exhibiting that $\sigma_{dc}(x = 2.5)/\sigma_{dc}(x = 0.75) = 9.65 \times 10^{2}$.

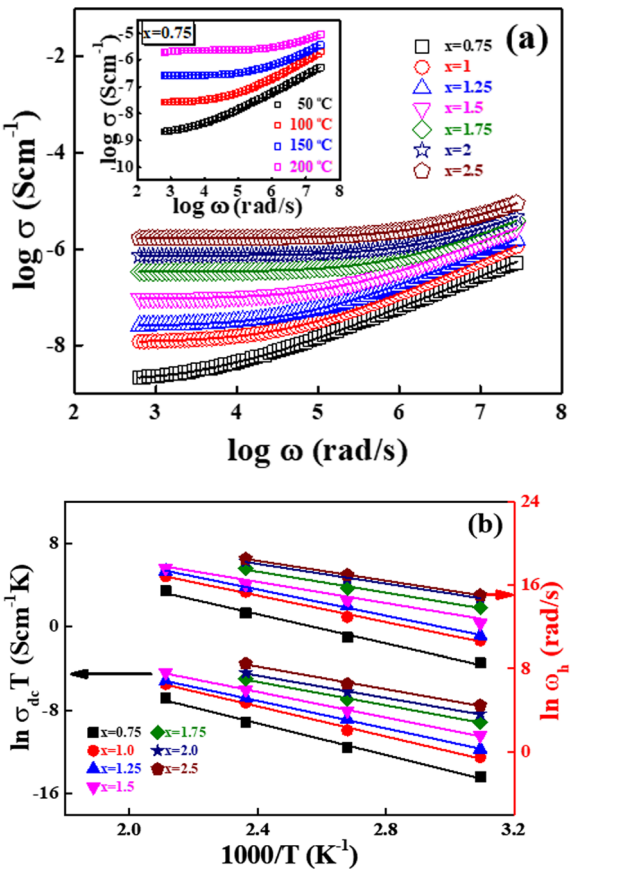

Fig. 3 Conductivity analysis; (a) frequency spectra of the real conductivity $\sigma(\omega)$ for xLi_2O-AGPO ($x = 0.75, 1.0, 1.25, 1.5, 1.75, 2.0, 2.5$) glasses at 50 °C. The inset of the figure shows the conductivity spectra for $x = 0.75$ at various temperatures. (b) Reciprocal temperature dependence of the dc conductivity and the hopping frequency ω_h obtained from the universal power law analysis in eqn (3). The solid lines indicate that ω_h obeys the Arrhenius relationship $\omega_h = \omega_0 \exp\left(-\frac{E_h}{k_BT}\right)$.

Meanwhile, the result in the inset shows that the dc conductivity $\sigma_{dc} = 1.73 \times 10^{-9}$ S cm^{-1} at 50 °C increases to 2.22×10^{-6} S cm^{-1} at 200 °C. The results indicate that the conductivity values become almost 10^3 times higher with increasing content of Li_2O as well as increasing temperature. Consequently, the results from the power-law analysis are consistent with those obtained from the Cole–Cole representation.

The average value of exponent s in eqn (5) is 0.70 ± 0.02 for xLi_2O-AGPO glasses, which are the obtained values from the fit at various temperatures and at several contents of Li_2O. That is, the values of s were found to be independent of temperature as well as composition in xLi_2O-AGPO glasses. As shown in Fig. 3(b), the reciprocal temperature dependence of ω_h follows the Arrhenius relationship:

$$\omega_h = \omega_0 \exp\left(-\frac{E_h}{k_BT}\right), \quad (6)$$

where ω_0 is a pre-exponential factor and E_h is the hopping energy at the onset frequency ω_h of Jonscher's power law in eqn (5). The obtained dc activation energy and hopping energy of xLi$_2$O-AGPO decreased from $E_{dc}^{J} = 0.66$ eV and $E_h = 0.61$ eV for $x = 0.75$ glass to $E_{dc}^{J} = 0.47$ eV and $E_h = 0.41$ eV for $x = 2.5$ glass, obtained from the least square straight-line fits of the experimental data to eqn (5) and (6).

For the calculation of the charge carrier concentration n_c and the mobility μ, we present the composition dependent dc conductivity σ_{dc} and hopping frequency ω_h for the xLi$_2$O-AGPO glasses in Table 1. The similarity of the activation energies calculated from the Cole–Cole representation and the universal power-law formalism implies that the activation energy is an appropriate parameter for describing the electrical relaxation and conduction mechanisms. It is emphasized that the ion transport mechanism is based on the hopping process of ions through the sub-transport in the multiple trapping percolation clusters with the low-dimensional conduction pathway.[23]

How many charge carriers contribute to the ionic conductivity and how much their mobility contributes are fundamental questions in glass systems. The frequency dependence of conductivity suggested by Jonscher in eqn (5) is sometimes referred to as the Almond–West (AW) formula. Almond and West identified the crossover frequency ω_h with a hopping rate of the mobile ions in a solid. Using the values of ω_h and σ_{dc}, which are obtained from the experiment and analysis, with the Nernst–Einstein relationship, the concentration of mobile ions n_c (ref. 25) can be obtained as follows:

$$n_c = \frac{6\, k_B T}{q^2 \lambda^2} \frac{\sigma_{dc}}{\omega_h}. \quad (7)$$

In this expression, q is the charge of the mobile ion, λ denotes the elementary hopping distance, k_B is the Boltzmann constant, and T is the temperature. The elementary hopping distance in the solid is 2–3 Å, and we have used a fixed value of 3 Å for all samples in calculating the carrier concentration.[31]

The carrier mobility μ can be calculated from the dc conductivity for solid materials, which is given by

$$\sigma_{dc} = n_c q \mu. \quad (8)$$

The use of the effective concentration of charge carriers n_c in eqn (7) yields μ in eqn (8) and the results are summarized in Table 1.

The calculated charge carrier concentration exhibits a trend consistent with the variation in Li$_2$O content, increasing from 3.91×10^{20} to 5.81×10^{20} cm^{-3} as $0.75 \leq x \leq 2.5$. Meanwhile, when the Li$_2$O content increases from $x = 0.75$ to 2.75, both the dc conductivity and the charge carrier mobility increase by approximately three orders of magnitude, from 1.73×10^{-9} to 1.67×10^{-6} S cm^{-1} and from 2.77×10^{-11} to 1.67×10^{-8} cm^2 V^{-1} s^{-1}, respectively.

The relationship between σ_{dc}, n_c, and μ is presented in Fig. 4, where the calculated σ_{dc} from the measured data is plotted *versus* the x content. The inset in Fig. 4 shows that the calculated mobility μ is plotted *versus* the x content. Meanwhile, the calculated charge carrier concentration n_c increases proportionally with the mole ratio of x in the xLi$_2$O-AGPO glasses. The result indicates that the exponential increase in dc conductivity is caused by the mobility rather than by the charge carrier concentration.

The results show that the conducting channels are widely open for long-range cooperative hopping due to the increase in NBO sites because of the depolymerization of the network. As a consequence, the ionic dc conductivity increases exponentially, as does the mobility in xLi$_2$O-AGPO glasses.

3.3. Relationship between Raman spectra and conductivity

Raman spectroscopy is a powerful tool for examining the phase composition of solid electrolytes and for probing local and

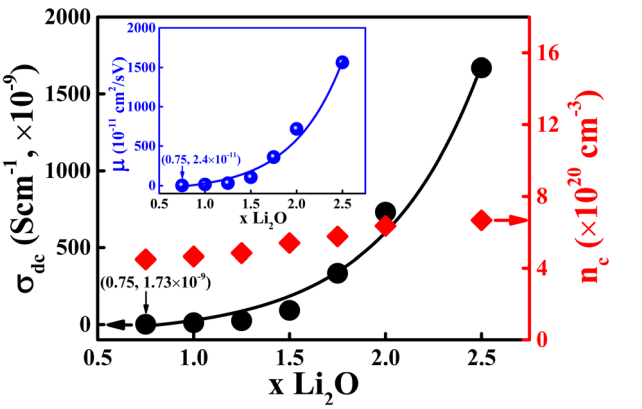

Fig. 4 Conductivity analysis; dc conductivity and charge carrier number density *vs.* lithium contents of the xLi$_2$O-AGPO ($x = 0.75$, 1.0, 1.25, 1.5, 1.75, 2.0, 2.5) glasses at $T = 50$ °C. The inset illustrates the variation of carrier mobility μ with Li$_2$O content at $T = 50$ °C.

Table 1 Calculated dc conductivity σ_{dc}, hopping frequency ω_h, concentration of charge carrier n_c, and mobility μ at $T = 50$ °C with the best fit values based on experimental and analysis parameters for xLi$_2$O–0.25Al$_2$O$_3$–1.5GeO$_2$–1.5P$_2$O$_5$ ($x = 0.75$, 1.0, 1.25, 1.5, 1.75, 2.0, 2.5) glasses

x	σ_{dc} (50 °C) (S cm^{-1})	ω_h (50 °C) (Hz)	n_c (50 °C) (cm^{-3})	μ (50 °C) (cm^2 s^{-1} V^{-1})
0.75	1.73×10^{-9}	5.12×10^{3}	3.91×10^{20}	2.77×10^{-11}
1.0	1.15×10^{-8}	3.29×10^{4}	4.05×10^{20}	1.77×10^{-10}
1.25	2.47×10^{-8}	6.78×10^{4}	4.22×10^{20}	5.52×10^{-10}
1.5	9.18×10^{-8}	2.26×10^{5}	4.70×10^{20}	1.22×10^{-9}
1.75	3.34×10^{-7}	7.70×10^{5}	5.02×10^{20}	4.16×10^{-9}
2.0	7.31×10^{-7}	1.53×10^{6}	5.54×10^{20}	8.25×10^{-9}
2.5	1.67×10^{-6}	3.33×10^{6}	5.81×10^{20}	1.80×10^{-8}

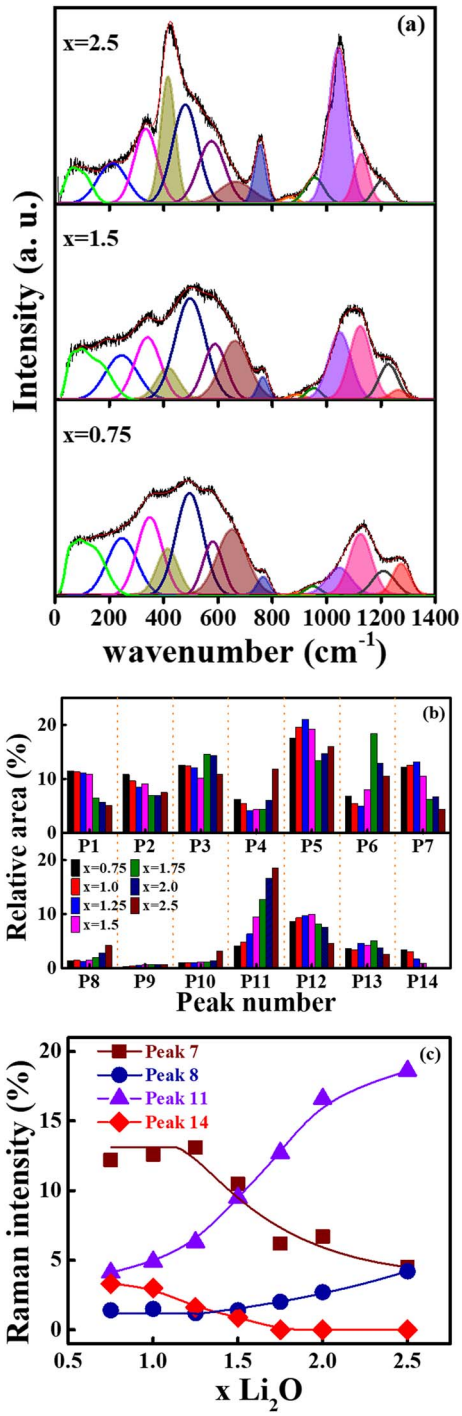

Fig. 5 (a) Deconvoluted Raman spectra of xLi$_2$O-AGPO (x = 0.75, 1.5, 2.5) glasses at 50 °C. Red solid line is the resultant curve fit obtained from several individual deconvoluted Gaussian bands. (b) Relative area ratio of Raman scattering intensity bands of xLi$_2$O-AGPO (x = 0.75, 1.0, 1.25, 1.5, 1.75, 2.0, 2.5) glasses at 50 °C. (c) Several peaks of Raman scattering intensity with Li$_2$O content at 50 °C.

cooperative structural changes. Fig. 5(a) presents the Raman spectra of xLi$_2$O-AGPO glasses with x = 0.75, 1.5, and 2.5 measured at room temperature. The reduced spectra were deconvoluted using Gaussian functions to assign the vibrational modes. The baseline correction was performed using an exponential decay function to remove background contributions. For comparison, the spectra were also processed using a Bose–Einstein population factor, and no significant differences in the overall spectral features or trends were observed. The Raman spectra of xLi$_2$O-AGPO glasses exhibit two characteristic spectral bands: (i) a low-frequency band below 800 cm^{-1}, which is mainly associated with the bending modes of (P, Ge, Al)–O polyhedra, chains and ring units. In addition, the Boson peak arising from cooperative vibrational motion appears in the frequency range below ~200 cm^{-1}. (ii) A high-frequency band above 800 cm^{-1}, which is attributed to the internal stretching modes of germanate and phosphate polyhedral units.

Fig. 5(a) shows the Raman spectra, in which broad bands are observed at 69–103 (P1), 202–247 (P2), 331–349 (P3), 418 (P4), 467–498 (P5), 568–589 (P6), 655–670 (P7), 759–771 (P8), 864–890 (P9), 949–955 (P10), 1047–1054 (P11), 1120–1133 (P12), 1207–1227 (P13), and 1269–1280 cm^{-1} (P14). The relative intensities of the Raman bands for the xLi$_2$O-AGPO glasses in Fig. 5(b) and the corresponding assignments of vibrational units are summarized in Table 2. Fig. 5(c) shows the composition dependence of the fractional intensity, for selected Raman bands (P7, P8, P11, and P14) in xLi$_2$O-AGPO glasses.

The broad band observed below ~200 cm^{-1} (P1) is assigned to the Boson peak, which is characteristic of disordered glassy systems.[32–34] The band at 202–247 cm^{-1} (P2) is attributed to the Ge–O–Ge bending mode of Q^2 tetrahedral units.[35] The bands appearing between 331 and 349 cm^{-1} (P3) are associated with Ge deformation motions within the network as well as O–P–O bending vibrations related to Q^2 phosphate units.[36,37] The peak at 418 cm^{-1} (P4) originates from the symmetric stretching vibrations of bridging oxygens in six-membered GeO$_4$ rings (Ge–O–Ge).[36] The band in the range of 467–498 cm^{-1} (P5) is attributed to O–P–O bending vibrations in Q^2 units, although contributions from O–P–O bending of Q^0 units or translational modes of Ge^{4+} cations have also been reported in this region.[38–40] The band centered around 580 cm^{-1} (P6) is assigned to Ge–O–P bending modes associated with GeO$_4$ structural units.[41] The bands near 655–670 cm^{-1} (P7) are mainly attributed to Ge–O–P bending modes involving GeO$_6$ groups.[41] According to Das *et al.*, the increased oxygen crowding around GeO$_6$ units hinders Ge–O–P bending, resulting in higher vibrational frequencies.[41] This interpretation is consistent with the observed decrease in the relative intensity of P7 with increasing x content, as shown in Fig. 5(b). Additionally, the P7 band may also include contributions from P–O–P bending vibrations in phosphate chains.[24] These observations are consistent with the NMR results reported by Schöder *et al.*, which indicate an increase in Ge–O–P connectivity accompanied by a reduction in P–O–P linkages.[42] The band in the range of 750–770 cm^{-1} (P8) is assigned to the symmetric stretching vibrations of P–O–P bridging oxygens between two phosphate tetrahedra, characteristic of Q^1 species.[43] A contribution from Ge–O–P stretching vibrations has also been reported near this frequency.[36] The band near 880–890 cm^{-1} (P9) is attributed to Ge–O stretching vibrations in GeO$_4$ tetrahedra.[44,45] The shoulder observed around 944–955 cm^{-1} (P10) indicates the presence of isolated PO$_4^{3-}$ groups (Q^0 units) and is associated with symmetric

Table 2 Raman peak band assignments and their relative area of Raman spectral components for $x$$Li_2O$–0.25$Al_2O_3$–1.5$GeO_2$–1.5$P_2O_5$ ($x$$Li_2O$-AGPO; x = 0.75, 1.0, 1.25, 1.5, 1.75, 2.0, 2.5) glasses

Peak no.	Peak frequency (cm^{-1}) (relative area (%))							Raman assignments [and references]
	$x = 0.75$	$x = 1.0$	$x = 1.25$	$x = 1.5$	$x = 1.75$	$x = 2.0$	$x = 2.5$	
P1	93 (11.5)	97 (11.3)	103 (11.0)	99 (10.9)	100 (6.5)	69 (5.7)	69 (5.2)	Boson peak[33–35]
P2	247 (10.8)	240 (9.6)	240 (8.5)	245 (9.1)	204 (6.9)	202 (6.9)	211 (7.5)	Ge–O–Ge bending (Q^2) tetrahedra[36]
P3	349 (12.6)	344 (12.4)	342 (12.0)	341 (10.1)	331 (14.5)	333 (14.3)	334 (10.9)	Ge deformation,[37] O–P–O (Q^2) bending[38]
P4	418 (6.2)	418 (5.5)	418 (4.2)	418 (4.4)	418 (4.5)	419 (6.1)	419 (11.8)	Ge–O–Ge symmetric stretching in the GeO_4 ring[37]
P5	496 (17.6)	498 (19.6)	498 (21.0)	498 (19.2)	467 (13.3)	479 (14.7)	480 (16.1)	O–P–O bending (Q^0),[39,40] in-chain O–P–O stretching (Q^2)[41]
P6	581 (6.8)	583 (5.5)	585 (5.0)	589 (8.1)	568 (18.4)	576 (12.9)	576 (10.5)	Ge–O–P bending for GeO_4 (ref. 42)
P7	655 (12.2)	655 (12.6)	655 (13.1)	667 (10.5)	670 (6.2)	670 (6.7)	670 (4.5)	P–O–P bending in chain 24, Ge-O-P bending for GeO_6 (ref. 42)
P8	771 (1.4)	770 (1.5)	771 (1.2)	770 (1.4)	765 (2.0)	763 (2.7)	759 (4.2)	Ge–O–P stretching,[37], P–O–P symmetric stretching (Q^1)[44]
P9	890 (0.3)	890 (0.4)	890 (0.5)	890 (0.6)	890 (0.7)	890 (0.6)	864 (0.6)	Ge–O vibration in GeO_4 (ref. 45 and 46)
P10	950 (1.0)	950 (1.0)	949 (1.0)	952 (1.1)	950 (1.1)	950 (1.3)	955 (3.1)	O–P–O stretching (Q^0),[38] P–O–Ge_4 stretching[42]
P11	1050 (4.1)	1050 (4.9)	1050 (6.3)	1054 (9.5)	1050 (12.7)	1050 (16.6)	1047 (18.6)	PO_2 symmetric stretching (Q^1)[50]
P12	1130 (8.6)	1125 (9.3)	1124 (9.7)	1129 (9.9)	1120 (8.1)	1129 (7.6)	1133 (4.6)	O–P–O symmetric stretching (Q^2)[51,52]
P13	1210 (3.6)	1210 (3.4)	1220 (4.6)	1227 (4.3)	1216 (5.1)	1216 (3.7)	1207 (2.6)	P–O symmetric stretching (Q^1)[53]
P14	1280 (3.3)	1268 (3.0)	1270 (1.6)	1269 (0.9)	X	X	X	O–P–O asymmetric stretching (Q^2),[51] metaphosphate $(PO_3)^-$ (Q^2)[54]

stretching vibrations of O–P–O non-bridging oxygens or P–O–Ge stretching modes.[37,41,46] The band centered near 1050 cm^{-1} (P11) is assigned to P–O^- valence vibrations in pyrophosphate groups ($P_2O_7^{4-}$), as well as PO_2 stretching modes associated with non-bridging oxygens in Q^1 tetrahedra.[47–49] The intensity of this band increases systematically with increasing x content. The dominant band observed near 1120–1133 cm^{-1} (P12) is attributed to the symmetric stretching vibrations of non-bridging oxygens in Q^2 phosphate units.[50,51]

The bands observed near 1207–1227 cm^{-1} (P13) are assigned to the symmetric stretching vibrations of P–O bonds in Q^1 phosphate tetrahedra.[52] The high-frequency shoulder appearing at 1269–1280 cm^{-1} (P14) is attributed to $(PO_3)^-$ units associated with metaphosphate groups or to the asymmetric O–P–O stretching vibrations of Q^2 tetrahedra.[50,53] The presence of this band indicates small amounts of metaphosphate (Q^2) linkages coexisting with the predominant pyrophosphate structure, consistent with an O/P ratio ≥3.5.

With increasing x content, the intensities of the bands at 1120–1133 cm^{-1} (P12) and 1269–1280 cm^{-1} (P14) progressively decrease, while those of the bands at ~750–770 cm^{-1} (P8) and ~1050 cm^{-1} (P11) increase. These changes indicate that the incorporation of Li^+ ions into the $x$$Li_2O$-AGPO glass system modifies the phosphate network through a transformation from metaphosphate (Q^2) to pyrophosphate (Q^1) linkages. The shift of the P–O–P vibrational modes toward lower wavenumbers, particularly for the P8 band, can be attributed to changes in the local bonding environment associated with depolymerization, where the mass contribution of phosphorus dominates relative to that of oxygen in O–P–O units. Overall, the addition of Li_2O promotes the formation of pyrophosphate units *via* depolymerization of metaphosphate chains, leading to the generation of additional non-bridging oxygen (NBO) sites. Henderson and Amos reported that alkali germanophosphate glasses can be regarded as comprising separate germanate and phosphate subnetworks, with depolymerization occurring predominantly through the formation of Q^2 and Q^1 PO_4 tetrahedra within the phosphate network rather than the germanate framework.[50] The creation of NBO sites facilitates Li^+ ion migration by providing favorable conduction pathways. Consistent with this interpretation, increasing Li/P ratios in $x$$Li_2O$-AGPO glasses result in progressively depolymerized phosphate structures,[52] which in turn lead to enhanced ionic conductivity with increasing x content.

For compositions with $x \geq 1.75$, the relative intensity of the Ge–O–P bending mode associated with GeO_4 structural units near 580 cm^{-1} (P6) initially increases and then decreases with further increasing x content. In contrast, the intensity of the band near 655–670 cm^{-1} (P7) for $x \geq 1.75$ is lower than that observed for compositions with $0.75 \leq x \leq 1.5$. Henderson and Amos proposed that the connectivity between phosphate and germanate components in alkali germanophosphate glasses is mediated through O–Li–O bridges, in which Li^+ ions are coordinated by multiple oxygen atoms, including bridging oxygens (BOs) associated with GeO_4 tetrahedra and non-bridging oxygens (NBOs) associated with PO_4 tetrahedra.[50] They further suggested that the formation of three-membered GeO_4 rings provides suitable interstitial sites for accommodating alkali cations, with BOs associated with these rings acting as coordination sites. According to this model, Li^+ ions simultaneously coordinate to NBOs of phosphate tetrahedra and BOs of germanate tetrahedra. The observed changes in the intensities of the P6 and P7 bands for $x \geq 1.75$ therefore suggest a reduction in the number of suitable interstitial sites available for alkali

cation accommodation with increasing x content in $x$$Li_2O$-AGPO glasses. Although the formation of extended phosphate chains may promote long-range ion hopping pathways, the number of effectively accommodated Li^+ ions gradually decreases at higher x values.

Pershina *et al.* suggested that the loosening of the glass network in Li_2O–Al_2O_3–GeO_2–SiO_2–P_2O_5 glasses originates from an increase in modifier content (Li_2O + Al_2O_3) accompanied by a decrease in glass formers (GeO_2 + SiO_2 + P_2O_5).[54] It is well established that the incorporation of metal cations into phosphate glasses leads to the cleavage of P–O–P bonds and the formation of P–O–M (M = metal) linkages. Brow *et al.* reported that, with increasing Al content in $Al(PO_3)_3$-based systems, P–O–Li^+ bonds are progressively replaced by P–O–Al bonds, accompanied by a reduction in P–O–P linkages.[55] More recently, Schröder *et al.* demonstrated in $Li_{1+x}Al_xGe_{2-x}(PO_4)_3$ (LAGP) glass-ceramic systems that the formation of P–O–Al and P–O–Ge linkages is favored over P–O–P and Ge–O–Al linkages.[42] They further showed that the local substitution of Ge^{4+} by Al^{3+} leads to an expansion of the octahedral sites, with AlO_6 polyhedra being noticeably larger than GeO_6 units in the NASICON-type $LiGe_2(PO_4)_3$ structure, resulting in an increase of the local P⋯Al distance by approximately 7% compared to the Ge⋯P distance. Similarly, Moguš-Milanković *et al.* reported that the addition of Al_2O_3 to alkali alumina phosphate glasses promotes the replacement of alkali metaphosphate units by aluminum metaphosphate, where $Al(OP)_6$ units act as cross-linking centers between phosphate chains, leading to an increase in P–O–Al linkages and the formation of extended phosphate networks.[49] Consistent with these observations, an increase in x content in $x$$Li_2O$-AGPO glasses results in a progressive broadening of the strong Raman band at ~1050 cm^{-1} (P11), indicating enhanced structural disorder. This trend is in good agreement with the disorder inferred from the Cole–Cole analysis. As the degree of structural disorder increases, the calculated Li^+ mobility (μ) listed in Table 1 also increases systematically with increasing x content in $x$$Li_2O$-AGPO glasses.

The evolution of the Raman spectra in $x$$Li_2O$-AGPO glasses can be correlated with changes in the structural network as a function of the O/P ratio. Brow *et al.* reported that octahedrally coordinated Al species are predominant in phosphate glasses with O/P ratios below 3.5, corresponding to the pyrophosphate structural limit, whereas tetrahedrally coordinated Al becomes dominant at O/P ratios exceeding 3.5.[55] For the $x$$Li_2O$-AGPO glass with x = 2.5, the O/P ratio is expected to exceed 3.5, which is consistent with the pronounced changes observed in the Raman spectra, particularly for the bands at ~418 cm^{-1} (P4) and 1047–1054 cm^{-1} (P11). As discussed above for glasses with higher x content, the cross-linking of phosphate chains leads to increased overlap in the distribution of potential barriers, resulting in a reduction of the effective potential well depths for Li^+ ion migration. This evolution of the potential energy landscape implies a progressive lowering of the activation barriers associated with long-range ion transport. Accordingly, the dc activation energy decreases systematically from 0.68 ± 0.02 eV to 0.47 ± 0.03 eV as the x content increases from 0.75 to 2.5.

4. Conclusions

$x$$Li_2O$–0.25$Al_2O_3$–1.5$GeO_2$–1.5$P_2O_5$ ($x$$Li_2O$-AGPO; x = 0.75–2.5) glasses were synthesized by the plate quenching method. Experimental and analysis results demonstrate that the dc ionic conductivity increases, while the dc activation energy decreases systematically with increasing Li_2O content in the $x$$Li_2O$-AGPO glasses. The calculated charge carrier concentration n_c increases proportionally with the Li_2O mole fraction x, whereas the ionic dc conductivity exhibits an exponential increase, primarily governed by the enhanced Li^+ mobility. The improved Li^+ transport is attributed to the formation of non-bridging oxygen (NBO) sites arising from depolymerization of the phosphate network. At higher Li_2O contents, the formation of extended phosphate chains leads to a shallower potential energy landscape for Li^+ migration, resulting in reduced activation energies. These results highlight the strong correlation between the glass network structure and ionic transport dynamics, providing important insights for the design of functional glassy solid electrolytes for electrochemical energy storage applications.

Conflicts of interest

There are no conflicts to declare.

Data availability

The data supporting this article have been included as part of the supplementary information (SI). Supplementary information: complex impedance plane plots, conductivity and Raman spectra, and model fitting parameters. See DOI: https://doi.org/10.1039/d5ta09357k.

Acknowledgements

This work was supported by the National Research Foundation of Korea (NRF) grant funded by the Korea government (MSIT) (No. RS-2023-00276591, and RS-2021-NR062805). The work was also supported by the Ministry of Education (RS-2021-NR066344), Republic of Korea.

References

1 J. B. Goodenough and Y. Kim, *Chem. Mater.*, 2019, **22**, 587–603.
2 M. Armand and J.-M. Tarascon, *Nature*, 2008, **451**, 652–657.
3 Y. Kobayashi, S. Seki, A. Yamanaka, M. Miyashiro, Y. Mita and T. Iwahori, *J. Power Sources*, 2005, **146**, 719–722.
4 J. Schwenzei, V. Thangadurai and W. Weppner, *J. Power Sources*, 2006, **154**, 232–238.
5 L. He, Q. Sun, C. Chen, J. A. S. Oh, J. Sun, M. Li, W. Tu, H. Zhou, K. Zeng and L. Lu, *ACS Appl. Mater. Interfaces*, 2019, **11**, 20895–20904.
6 Y. Zhang, H. Liu, Z. Xie, W. Qu, D. J. Freschi and J. Liu, *Adv. Funct. Mater.*, 2023, **33**, 2300973.

7 X. Xu, Z. Wen, X. Wu, X. Yang and Z. Gu, *J. Am. Ceram. Soc.*, 2007, **90**(9), 2802–2806.
8 P. H. Kuo and J. Du, *J. Phys. Chem. C*, 2019, **123**, 27385–27398.
9 Y. Nikodimos, L. H. Abrha, H. H. Weldeyohannes, K. N. Shitaw, N. T. Temesgen, B. W. Olbasa, C.-J. Huang, S.-K. Jiang, C.-H. Wang, H.-S. Sheu, S.-H. Wu, W.-N. Su, C.-C. Yang and B. J. Hwang, *J. Mater. Chem. A*, 2020, **8**, 26055–26065.
10 S. Li, J. Cai and Z. Lin, *Solids State Ion.*, 1988, **28–30**, 1265–1270.
11 S. V. Pershina, B. D. Antonov, A. S. Farlenkov and E. G. Vovkotrub, *J. Alloys Compd.*, 2020, **835**, 155281.
12 C. G. Baek, H. W. Choi and Y. S. Yang, *J. Alloys Compd.*, 2014, **615**, 745–748.
13 M. C. Ersundu, A. E. Ersundu, M. T. Soltani and M. Baazouzi, *Ceram. Int.*, 2017, **43**, 491–497.
14 C. G. Baek, M. Kim, O. H. Kwon, H. W. Choi and Y. S. Yang, *Cryst. Growth Des.*, 2017, **17**, 5684–5690.
15 S. W. Martin, *J. Am. Ceram. Soc.*, 1991, **74**, 1767–1784.
16 D. Ravaine and J. L. Souquet, *Phys. Chem. Glasses*, 1977, **18**, 27–31.
17 J. L. Souquet, M. L. F. Nascimento and A. C. M. Rodrigues, *J. Chem. Phys.*, 2010, **132**, 034704.
18 E. F. Hairetdinov, N. F. Uvarov, H. K. Patel and S. W. Martin, *Phys. Rev. B:Condens. Matter Mater. Phys.*, 1994, **50**, 13259–13266.
19 M. A. T. Marple, H. Avila-Paredes, S. Kim and S. Sen, *J. Chem. Phys.*, 2018, **148**, 204507.
20 A. Bunde, M. D. Ingram and P. Maass, *J. Non-Cryst. Solids*, 1994, **172–174**, 1222–1236.
21 D. L. Sidebottom, P. F. Green and R. K. Brow, *Phys. Rev. B:Condens. Matter Mater. Phys.*, 1995, **51**, 2770–2776.
22 J. Swenson and St. Adams, *Phys. Rev. Lett.*, 2003, **90**, 155507.
23 Y. H. Rim, M. Kim, J. E. Kim and Y. S. Yang, *N. J. Phys.*, 2013, **15**, 023005.
24 C. G. Baek, Y. H. Rim and Y. S. Yang, *J. Alloys Compd.*, 2022, **924**, 166523.
25 J. C. Dyre, P. Maass, B. Roling and D. L. Sidebottom, *Rep. Prog. Phys.*, 2009, **72**, 046501.
26 B. Roling, C. Martiny and S. Bruckner, *Phys. Rev. B:Condens. Matter Mater. Phys.*, 2001, **63**, 214203.
27 Y. H. Rim, M. Kim, C. G. Baek and Y. S. Yang, *J. Alloys Compd.*, 2020, **827**, 154253.
28 E. Barsoukov and J. R. Macdonald, *Impedance Spectroscopy, Third Ed*, John Wiley & Sons Inc., New Jersey, 2017.
29 J. R. Macdonald, *Solids State Ion.*, 1984, **13**, 147–149.
30 C. León, A. Rivera, A. Várez, J. Sanz, J. Santamaria and K. L. Ngai, *Phys. Rev. Lett.*, 2001, **86**, 1279–1282.
31 P. Posch, S. Lunghammer, S. Berendts, S. Ganschow, G. J. Redhammer, A. Wilkening, M. Lerch, B. Gadermaier, D. Rettenwander and H. M. R. Wilkening, *Energy Storage Mater.*, 2020, **24**, 220–228.
32 E. Courtens, M. Foret, B. Hehlen, B. Rufflé and R. Vacher, *J. Phys.: Condens. Matter*, 2003, **15**, S1279–S1290.
33 N. S. Shcheblanov, L. Giacommazzi, M. E. Povarnitsyn, S. Kohara, L. Martin-Samos, G. Mountjoy, R. J. Newport, R. C. Haworth, N. Richard and N. Ollier, *Phys. Rev. B*, 2019, **100**, 134309.
34 P. Tarte, A. Rulmont and C. Merckaert-Ansay, *Spectrochim. Acta, Part A*, 1986, **42**, 1009–1016.
35 E. I. kamitsos, Y. D. Yiannopoulos, M. A. karakassides, G. D. Chryssikos and H. Jains, *J. Phys. Chem.*, 1996, **100**, 11755–11765.
36 S. Kumar, S. Murugavel and K. J. Rao, *J. Phys. Chem. B*, 2001, **105**, 5862–5873.
37 B. W. Stuart, C. A. Grant, G. E. Stan, A. C. Popa, J. J. Titman and D. M. Grant, *J. Mech. Behav. Biomed. Mater.*, 2018, **82**, 371–382.
38 A. R. Zanatta, *Results Phys.*, 2020, **19**, 103500.
39 A. Moguš-Milanković, A. Šantić, S. T. Reis, K. Furic and D. E. Day, *J. Non-Cryst. Solids*, 2004, **342**, 97–109.
40 S. Bano, A. R. Romero, T. Islam, D. M. Grant, I. Ahmed and T. Hussain, *J. Therm. Spray Technol.*, 2021, **30**, 1862–1874.
41 A. Das, P. S. R. Krishina, M. Goswami and M. Krishinan, *J. Solid State Chem.*, 2019, **271**, 74–80.
42 C. Schröder, J. Ren, A. Candida, M. Rodrigues and H. Eckert, *J. Phys. Chem. C*, 2014, **118**, 9400–9411.
43 G. Galleani, S. H. Santagneli, Y. Messaddeq, M. de Oliveira Jr and H. Eckert, *Phys. Chem. Chem. Phys.*, 2017, **19**, 21612–21624.
44 J. F. Scott, *Phys. Rev. B*, 1970, **1**, 3488–3493.
45 T. P. Mernagh and L.-G. Liu, *Phys. Chem. Miner.*, 1997, **24**, 7–16.
46 A. Moguš-Milanković, A. Šantić, S. T. Reis, K. Furic and D. E. Day, *J. Non-Cryst. Solids*, 2005, **351**, 3246–3258.
47 Y. Kowada, M. Tatsumisago and T. Minami, *J. Phys. Chem.*, 1989, **93**, 2147–2151.
48 R. K. Brow, *J. Non-Cryst. Solids*, 2000, **263–264**, 1–28.
49 A. Moguš-Milanković, A. Šantić, A. Gajović and D. E. Day, *J. Non-Cryst. Solids*, 2001, **289**, 204–213.
50 G. S. Henderson and R. T. Amos, *J. Non-Cryst. Solids*, 2003, **328**, 1–19.
51 P. Goj, M. Ciecińska, M. Szumera and P. Stoch, *J. Therm. Anal. Calorim.*, 2020, **142**, 203–209.
52 P. Stoch, A. Stoch, M. Ciecinska, I. Krakowiak and M. Sitarz, *J. Non-Cryst. Solids*, 2016, **450**, 48–60.
53 X. Fang, C. S. Ray, A. Moguš-Milanković and D. E. Day, *J. Non-Cryst. Solids*, 2001, **283**, 162–172.
54 S. V. Pershina, T. A. Kuznetsova, E. G. Vovkotrub and S. A. Belyakov, *Membranes*, 2022, **12**, 1245.
55 R. K. Brow, R. J. Kirkpatrick and G. L. Turner, *J. Am. Ceram. Soc.*, 1993, **76**, 919–928.

